Performance of the First G-APD Cherenkov Telescope evaluated using Crab Nebula Observations

Arbet-Engels, A.[4]**, Baack, D.**[1]**, Balbo, M.**[2]**, Biland, A.**[4]**, Blank, M.**[3]**, Bretz, T.**[4a]**,
Bruegge, K.**[1]**, Bulinski, M.**[1]**, Buss, J.**[1]**, Dmytriiev, A.**[2]**, Dorner, D.**[3]**, Einecke, S.**[1]**,
Elsaesser, D.**[1]**, Herbst, T.**[3]**, Hildebrand, D.**[4]**, Kortmann, L.**[1]**, Linhoff, L.**[1]**, Mahlke, M.**[4a]**,
Mannheim, K.**[3]**, Mueller, S. A.**[4]**, Neise, D.**[4]**, Neronov, A.**[2]**, Noethe, M.**[*1]**, Oberkirch, J.**[1]**,
Paravac, A.**[3]**, Rhode, W.**[1]**, Schleicher, B.**[3]**, Schulz, F.**[1]**, Sedlaczek, K.**[1]**, Shukla, A.**[3]**,
Sliusar, V.**[2]**, Walter, R.**[2]

[1]TU Dortmund, Experimental Physics 5, Otto-Hahn-Str. 4a, 44227 Dortmund, Germany
[2]University of Geneva, ISDC Data Center for Astrophysics Chemin d'Ecogia 16, 1290 Versoix, Switzerland
[3]Universität Würzburg, Institute for Theoretical Physics and Astrophysics, Emil-Fischer-Str. 31, 97074 Würzburg, Germany
[4]ETH Zurich, Institute for Particle Physics and Astrophysics, Otto-Stern-Weg 5, 8093 Zurich, Switzerland
Received: date / Accepted: date

Abstract The First G-APD Cherenkov Telescope (FACT) is an Imaging Air Cherenkov Telescope (IACT) located on the Canary Island of La Palma.

FACT pursues two main goals: It is the first IACT to use Silicon Photo Multipliers (SIPMs) to detect the faint flashes of Cherenkov lights induced by extensive air showers in the atmosphere. Using this technology, FACT monitors the brightest extragalactic sources of gamma-ray emission in the TeV range.

Using extensive simulations and observations of the so-called standard candle in gamma-ray astronomy, the Crab Nebula, the sensitivity of the telescope and the newly developed analysis chain is evaluated. This analysis chain uses only free and open source software and deploys modern machine learning techniques to solve the reconstruction tasks in gamma-ray astronomy. Special attention has been given to make the analysis easy to reproduce. The dataset is available for download from the image parameter level onwards and instructions how the reader can replicate the results are given at github.com/fact-project/performance-paper. A fifth of the used raw data has already been published and is available at fact-project.org/data.

Keywords FACT · Gamma-Ray Astronomy · Imaging Air Cherenkov Telescope

1 Introduction

The First G-APD Cherenkov Telescope (FACT) [1] is an Imaging Air Cherenkov Telescope, located at the Observatorio del Roque de los Muchachos on the Canary Island of La

---
[*]Corresponding author: maximilian.noethe@tu-dortmund.de
[a]also at RWTH Aachen

Fig. 1 The First G-APD Cherenkov Telescope in front of the MAGIC II Telescope at the Roque de los Muchachos observatory on the Canary Island of La Palma. [M. Nöthe]

Palma. As the first of its kind, FACT uses Silicon Photomultipliers (SiPMs) to detect the Cherenkov photons emitted by extensive air showers in the Atmosphere. Since first light in October 2011, the FACT Collaboration pursues the goals of continuously monitoring the brightest known sources of gamma-ray emission [2], showing the suitability of SiPMs for gamma-ray astronomy [3] and making FACT the first completely robotically operating IACT.

The performance of the telescope and the analysis chain is evaluated on Crab nebula observations taken between October 2013 and April 2014 as well as extensive simulations.

In Section 2 a brief overview of the FACT telescope is given. Section 3 introduces the datasets used for the analysis in this paper, both simulations and observations. In Section 4 the analysis chain is presented. Section 5 discusses the performance of FACT in terms of angular resolution, ef-
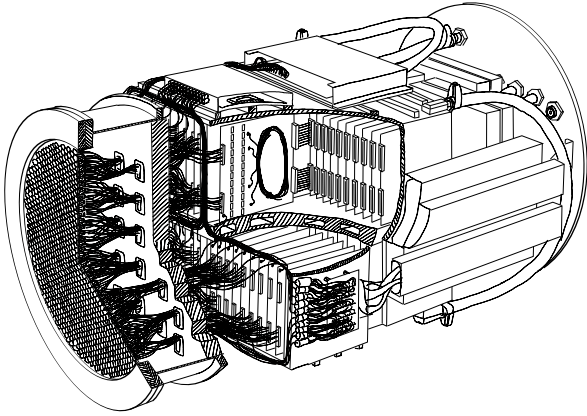
Fig. 2 Cutout drawing of the FACT camera. The hexagonal light-guides are glued to the circular window in the front of the camera. Each pixel's signal is fed into one of 40 boards containing the sampling electronics. Also visible are elements of the cooling mechanisms which keep the camera close to ambient temperature during operation. [S.A. Mueller]

fective area and detection sensitivity. Also the reconstructed spectral energy distribution of the Crab Nebula is shown. Section 7 concludes this paper.

2 The First G-APD Cherenkov Telescope

FACT's camera and mirrors are mounted on a refurbished alt-azimuth mount previously used by the HEGRA experiment. The new hexagonal mirrors have a total collection area of $9.51\,\mathrm{m}^2$ and are aligned to a hybrid shape between a Davies–Cotton-Reflector and a parabolic reflector [4]. The focal length of the optical system is $4.889\,\mathrm{m}$.

The imaging sensor of FACT comprises 1440 single Silicon Photomultiplier (SiPM) pixels of $3\,\mathrm{mm} \times 3\,\mathrm{mm}$. Each pixel is situated behind a light-guide with a hexagonal entrance window with a diameter of $9.5\,\mathrm{mm}$. FACT's total field of view is $4.5°$.

The most important part of the camera's electronic data acquisition is the Domino Ring Sampler 4 (DRS4) chip. The SiPM signals are continuously sampled by the DRS4 chip with a frequency of $2\,\mathrm{GHz}$.

A read-out is triggered by groups of 9 pixels. If the total signal in one group is above a given trigger threshold, the 300 voltage values recorded during the previous $150\,\mathrm{ns}$ are stored for each of the 1440 pixels in the camera. In nominal operating conditions, FACT triggers between 60 and 80 events per second. Each triggered event gets stored on disks at the telescope site from where the data will eventually get transferred to the main land.

Including dedicated calibration runs this leads to a total data volume of up to $0.5\,\mathrm{TB}$ per observed night.

Figure 2 shows a cutout drawing of the FACT camera.

3 Datasets used in the analysis

To determine the performance characteristics of FACT, observations as well as simulations are used. Simulations are needed, because in gamma-ray astronomy, there are no test-beams available to calibrate the detector response. Instead, extensive simulations are performed to obtain datasets with known truth values for the properties of the primary particle inducing the extensive air shower. The most important properties are the energy, direction and particle type of the primary.

For this analysis, Crab nebula observations taken between October 2013 and April 2014 with a total observation time of $91.1\,\mathrm{h}$ are used. Only observations with a zenith distance smaller than $30°$ and during dark night were selected. In total, the dataset contains just over 8 million events. The observations were carried out in wobble mode [5], using two positions with a distance of $0.6°$.

The simulations were performed using CORSIKA [6] to simulate the extensive air showers in the atmosphere and CERES [7] to simulate the detector.

Three types of simulations were performed:

1. Gamma rays from a point source observed in wobble mode.
2. Diffuse gamma rays, scattered over the field of view of FACT.
3. Diffuse protons, scattered over the field of view of FACT.

Gamma rays were simulated between $200\,\mathrm{GeV}$ and $50\,\mathrm{TeV}$ using a power law spectrum with a spectral index of -2.7 and a maximum scatter radius of $270\,\mathrm{m}$. Protons were simulated between $100\,\mathrm{GeV}$ and $200\,\mathrm{TeV}$ using the same power law, a viewcone of $5°$ and a maximum scatter radius of $400\,\mathrm{m}$. In total, 12 million gamma-ray and 720 million proton showers were simulated using CORSIKA. Of those showers, approximately 2 million point-source, 550 000 diffuse gamma rays and 500 000 protons triggered the telescope.

4 The FACT-Tools Analysis chain

Several preprocessing steps have to be performed on the FACT data, to get from the raw time series in each pixel to event wise parameters suitable for event reconstruction.

These steps are performed using the `FACT-Tools` [8], which was developed at TU Dortmund and ETH Zurich to perform these tasks. `FACT-Tools v1.0.0` [9] is used for the analysis presented in this paper.

In the following, each of the applied analysis steps is shortly introduced.
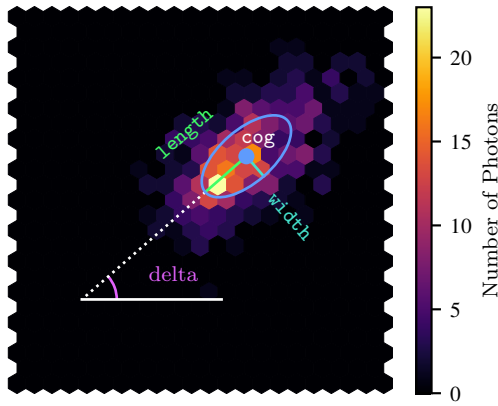
Fig. 3 The lower order Hillas parameters.

4.1 Preprocessing and Image Parameterization using FACT-Tools

DRS4 Calibration FACT is using the Domino Ring Sampler 4 [10] chip to sample the output signal of the SiPMs. The amplitude and timing of the sampled data has to be calibrated using measurements that are taken in between observations several times a night.

Artifact Removal Data sampled using the DRS4 chips shows two artifacts, that have to be removed before further processing: so called spikes are large increases in the time series for one or two adjacent values, jumps are a suddenly occurring shift in the baseline. These artifact are removed after the amplitude and time calibration steps are performed.

Signal Extraction From the calibrated time series in each pixel, two numbers are extracted: the number of photons and their mean arrival time. To estimate the number of photons, the time series is integrated for thirty values after the half-height of the maximum value. The rising edge of the pulse is fitted with a third order polynomial and the point of inflection is used as the mean arrival time. At this step, the date is often called an image.

Image Cleaning As a last step before the parameterization of the images, pixels which are not likely to contain Cherenkov photons are discarded using the following algorithm:

1. Find pixels containing more photons than an upper threshold t_1
2. Remove pixels with less than N neighbors above that threshold
3. Add neighbors of the remaining pixels that are above a lower threshold t_2
4. Remove pixels that have less than N neighbors with an arrival time inside a time limit Δt
5. Remove single pixels with less than N neighbors in the remaining pixels
6. Remove pixels that have less than N neighbor with an arrival time inside Δt

For this analysis, $t_1 = 5$ p.e., a lower threshold of $t_2 = 2.5$ p.e., $N = 2$, and $\Delta t = 5$ ns is used.

Image Parameterization The remaining pixels after the cleaning are used to calculate features that describe the image as single numbers.

The most well-known features come from the parameterization proposed by A. M. Hillas [11]. These features can be interpreted as a principal component analysis of the 2d light distribution. The standard deviations along the two components are called `length` and `width`, the orientation is given by the angle `delta` and the center of gravity. The total number of photons after cleaning is called `size`. These features are visualized in Figure 3.

Higher order moments, the skewness and kurtosis, are calculated along those components. The skewness along the main shower axis is especially important for estimating the source position of a gamma ray. The slope of the photon arrival times along the main shower axis is calculated using a linear regression.

To further describe the light distribution, so called concentrations are used. These are the number of photons in certain areas divided by `size`. The percentage of photons inside the Hillas ellipse, the percentage of photons in the brightest pixel, the two brightest pixels and the three pixels next to the center of gravity of the shower are calculated.

`num_pixel_in_shower` is the number of pixels after cleaning and the number of separated groups of pixels after the cleaning is called `num_islands`.

The percentage of light in the one and two outermost rings of pixels is called `leakage1` and `leakage2` and give an indication how well a shower image is contained in the camera.

Additionally, moments of the full arrival time and photon distribution are calculated.

4.2 Preselection of events

To remove hard to reconstruct events, e. g. events not fully contained in the field of view and to improve the agreement with simulations and observations, a few event selection cuts are performed before the final reconstruction steps.

The following selection cuts are used in this analysis:

- `num_pixel_in_shower` ≥ 10 to remove showers to small to reconstruct
- `num_islands` < 8 to remove noise events existing only in the observations and suppress hadron induced events.
- `length` < 70 and `width` < 35, both to suppress hadron induced events and improve observation/simulation agreement.

– `leakage1 < 0.6` and `leakage2 < 0.85` to suppress events that were not mostly contained in the field of view.

4.3 Event Reconstruction using Machine Learning

To solve the three main reconstruction tasks in gamma-ray astronomy – particle class, energy and direction, an open source software package called `aict-tools` has been developed [12], that makes use of machine learning algorithms of the Python package `scikit-learn` [13].

For the training of the machine learning models, the simulated point-like gamma rays are split into a training dataset which contains 30 % of the data and a dataset for evaluating the performance characteristics with the rest of the data. The training of each model is done in a 20-fold cross validation to estimate mean and uncertainty of performance characteristics describing the models.

For this analysis, a random forest regressor is trained on simulated point-source gamma-rays to estimate the energy of each particle. The cross-validated r^2-score of the model using 200 decision trees and a maximum depth of 15 is 0.817 ± 0.022 .

For the particle type classification, a random forest classifier trained to distinguish between showers induced by gamma rays and protons is used. The cross validated area under the ROC-curve for the random forest using 200 trees and a maximum depth of 15 is 0.873 ± 0.003 .

The reconstruction of the particle origin is performed using the *Disp-Method* [5, 14].

The Disp-Method simplifies the reconstruction task from a two-dimensional regression, e. g. x- and y-coordinate of the source position in the camera plane, to a one-dimensional regression and a binary classification. Based on the assumption, that the true source position lies somewhere on the main shower axis, a random forest regressor is trained on simulated diffuse gamma rays to estimate the distance between the center of gravity of the light distribution and the source position. This results in two possible solutions, one in either direction on the main shower axis. A random forest classifier is used to pick the correct solution.

For the regression part, an r^2-score of 0.664 ± 0.010 is achieved, while the accuracy of the sign classification reaches 0.755 ± 0.004 over the whole energy range.

5 Performance Evaluation

In this section, a number of characteristics describing the sensitivity of gamma-ray cherekov telescopes are discussed and evaluated on the simulated events as well as observations of the Crab Nebula.
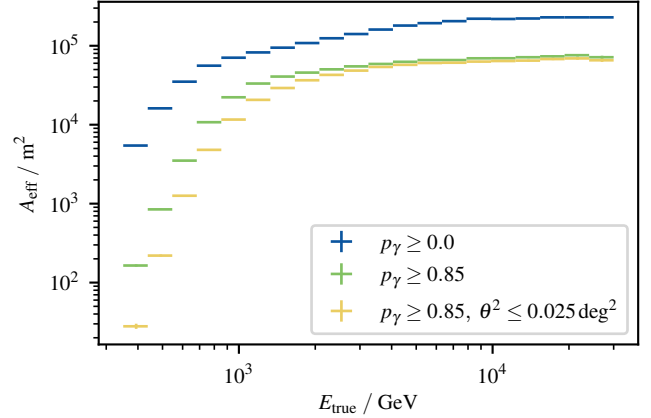

Fig. 4 Effective Area for three different steps of the analysis. First after the preselection cuts, second after applying the gamma/hadron-separation threshold, and third after applying both the gamma/hadron-separation and the source region selection.

5.1 Effective Area

The effective area describes equivalent size of a simple ground detector detecting the same number of particles.

The effective collection area is calculated in bins of the true, simulated energy of gamma-ray induced showers.

For each bin, the corresponding number of simulated gamma rays and detected gamma rays after different analysis steps and the scattering radius of the gamma rays are needed:

$$A_{\text{eff}} = \frac{N_{\text{detected}}}{N_{\text{simulated}}} \cdot 4\pi R^2 \tag{1}$$

As the number of detected events follows a binomial distribution, a shower is detected with a certain probability, the uncertainties are given as the 68 % central confidence interval of the binomial distribution.

The effective area for three different steps in the analysis is shown in Figure 4.

5.2 Angular Resolution

To judge the quality of directional reconstruction, the 68 %-quantile of the distance between the reconstructed and the true source position is calculated in bins of true energy. The plot is shown in Figure 5.

To give a better estimation on the angular resolution of the events selected in the analysis, only events with correctly classified sign of `disp` are shown, i.e. only the events where the random forest classifier chose the correct direction of the source position on the main shower axis. Events with wrongly classified sgn(`disp`) are reconstructed far away from their source and simply lost. This effect is visible in the effective area comparing the values before and after the source
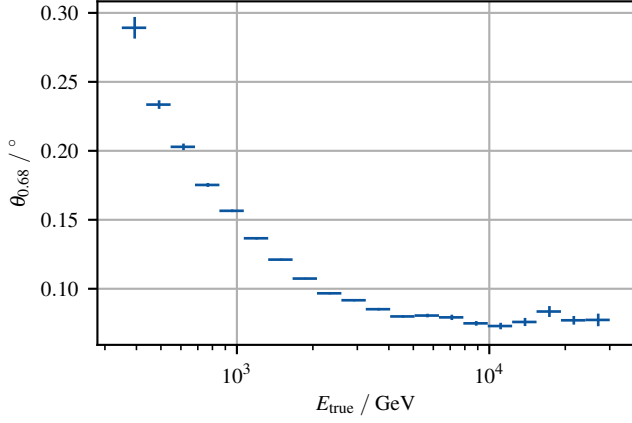
Fig. 5 Angular Resolution as the 68 % containment distance between reconstructed and true source position for simulated gamma ray events with correctly classified sgn(`disp`).
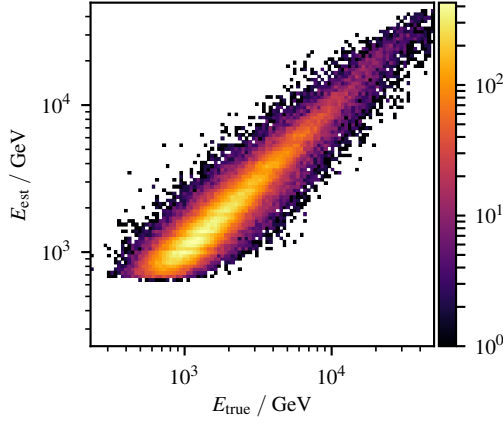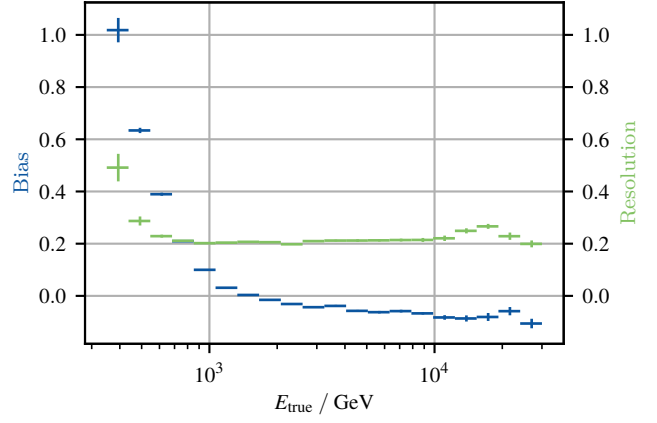

Fig. 7 Bias and resolution of the energy estimation as median and half width of the central 68 %-interval of the relative error Δ_{rel} for simulated gamma rays after event selection.

Fig. 6 Energy migration between estimated and true energy for simulated gamma rays after event selection.
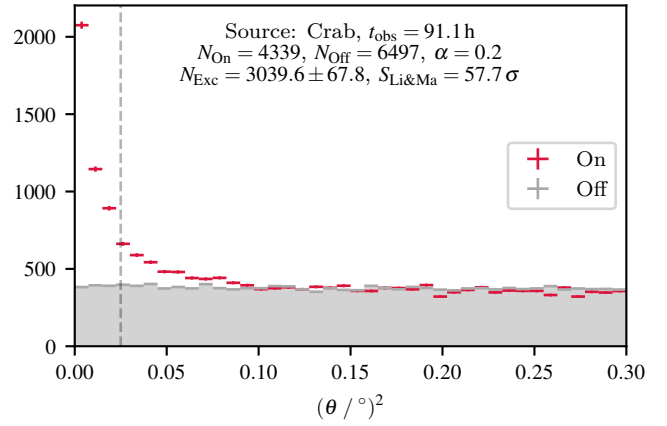

Fig. 8 Distribution of the squared distance between reconstructed and assumend source position, for the Crab Nebula (on) and the five background regions (off). A clear excess corresponding to significance of 57.7 σ is visible.

region selection. While the effect is negligible at higher energies, where the classification and regression perform best, the lower energies are affected more strongly.

5.3 Energy Bias and Resolution

The migration between true and estimated energy for simulated gamma-ray events after applying the source region and gamma/hadron selection cuts is shown in Figure 6.

The the relative error of the estimated energy is calculated for each event:

$$\Delta_{\mathrm{rel}} = \frac{E_{\mathrm{est}} - E_{\mathrm{true}}}{E_{\mathrm{true}}} \tag{2}$$

Per bin in true energy, the median and the interquantile distance of the central 68 %-quantile of Δ_{rel} are calculated, which are called bias and resolution respectively. The results are shown in Figure 7.

5.4 Detection of the Crab Nebula

Applying the analysis methods described before to the 91 h of Crab Nebula observations using the wobble observation mode [5] and using five off sources in the analysis for the background estimation results in a detection of the Crab Nebula with a significance of 57.7 σ according to the Li&Ma likelihood ratio test[15], which corresponds to $6\,\sigma/\sqrt{h}$. The integral sensitivity is calculated as the smallest flux as percentage of Crab Nebula flux, that would still yield a detection with a significance of 5 *sigma* in an observation time of 50 h.

The on region contains both signal and background events, while the off region only contains background. The size ratio of off and on region is α. The relative sensitivity s_{rel}, is the percentage of signal events, that still yields 5 sigma in 50 h of observation time. Both the signal and background events have to be scaled to the reference observation time of
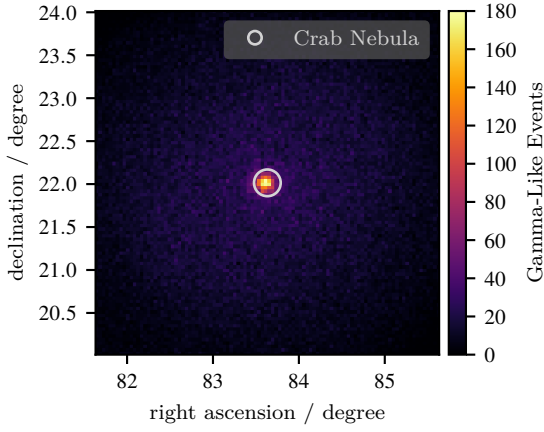
Fig. 9 Sky Map of the reconstructed source positions of the selected gamma ray candidates. The catalog coordinates of the Crab Nebula are shown as a gray circle.

50 h.

$$N_{\text{signal}} = N_{\text{on}} - \alpha N_{\text{off}} \tag{3}$$

$$\hat{N}_{\text{on}} = \frac{50\,\text{h}}{t_{\text{obs}}}(s_{\text{rel}} \cdot N_{\text{signal}} + \alpha N_{\text{off}}) \tag{4}$$

$$\hat{N}_{\text{off}} = \frac{50\,\text{h}}{t_{\text{obs}}} N_{\text{off}} \tag{5}$$

The significance according to Li & Ma is then solved numerically for s_{rel}:

$$S_{\text{Li\&Ma}}(\hat{N}_{\text{on}}, \hat{N}_{\text{off}}, \alpha) = 5 \tag{6}$$

Which results in 9.1 % Crab Units for $5\,\sigma$ in 50 h.

The distribution of θ^2, the squared distance between the reconstructed source position and the position of the Crab Nebula as well as the off source positions is shown in Figure 8.

The reconstructed positions of selected gamma ray candidates in the equatorial coordinate frame are shown together with the position of the Crab Nebula in Figure 9.

6 Spectral Unfolding

As it is not possible to measure physical attributes of particles directly and all observables suffer from limited resolution and possibly also a non-zero bias, unfolding is necessary to reconstruct the underlying distributions from the observables.

For the estimation of the energy spectrum of the Crab Nebula, a likelihood based unfolding method is used, that was implemented in the Python package `funfolding` [16] for [17], according to the methods described in [18].

A thin wrapper around `funfolding` to handle FACT data was developed [19] and used for this analysis.
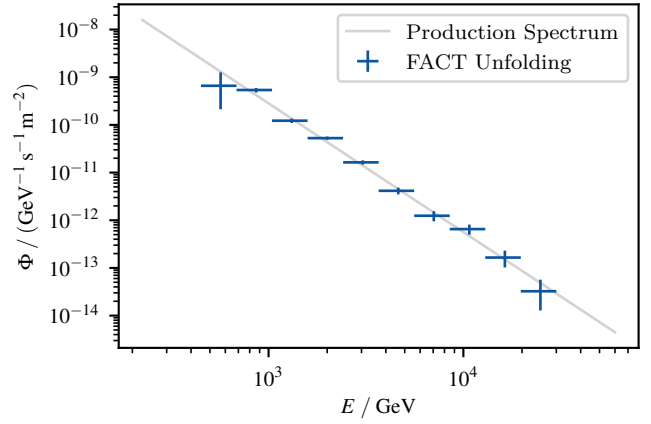

Fig. 10 Unfolding on simulated gamma-ray events.

The unfolding uses a poissonian maximum likelihood approach in bins of true and estimated energy. The measuring process is modeled by the folding integral

$$g(y) = \int A(x,y)f(x)\,\mathrm{d}x + b(y), \tag{7}$$

where $g(y)$ is the distribution of the observables y, $f(x)$ is the distribution of the searched for variable x, $A(x,y)$ is the detector response and $b(y)$ is any remaining background. In this case, y is the estimated gamma-ray energy and x is the true energy of the gamma rays.

To solve this inverse problem, the observed and true energy are discretized in equidistant bins in the logarithm of the energy. The folding integral becomes a matrix equation of the measured and true histograms as vectors and the detector response matrix:

$$\mathbf{g} = \mathrm{A} \cdot \mathbf{f} + \mathbf{b} \tag{8}$$

The detector response matrix is build from simulated gamma-ray events and $\mathbf{b}$ is estimated from the off positions. The right hand side of (8) is the expected value for each bin in the poissonian likelihood while the left hand side is the observed value for each bin in estimated energy. The Likelihood is sampled using a Markov-Chain-Monte-Carlo technique implemented by [20, 21]. The median of the sampled values used as estimator for the true value und the $1 - \sigma$-quantiles are used for the uncertainties. Dividing the estimation of $\mathbf{f}$ by the effective area $A_{\text{eff},i}$, the bin width w_i and the observation time t_{obs} finally gives the differential photon flux of the source for each energy bin:

$$\Phi_i = \frac{f_i}{t_{\text{obs}} \cdot A_{\text{eff},i} \cdot w_i}, \quad [\Phi] = \text{GeV}^{-1}\,\text{s}^{-1}\,\text{m}^{-2} \tag{9}$$

Unfolding, as an ill-posed problem, can show unphysical oscillations due to the condition of the detector response matrix. This can be reduced by applying Tikhonov regularization, which suppresses large second order derivatives. The regularization could be applied to the logarithm of the event
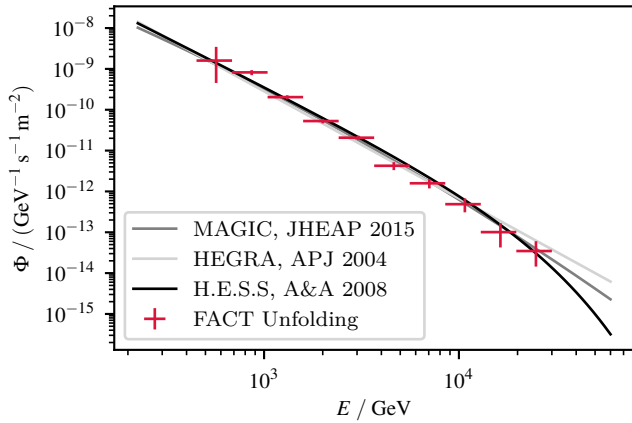
Fig. 11 Crab Nebula energy spectrum as result of the unfolding presented in this work compared to spectra published by the MAGIC [22] and HEGRA [23] collaborations.

spectra divided by the effective area, which is expected to be monotonic. However, due to the size of the given dataset, no regularization was necessary. Figure 10 shows that the unfolding reproduces the production spectrum of the simulated events.

The final result for the unfolding of the Crab Nebula observations is shown in Figure 11, together with spectra published by the MAGIC and HEGRA collaborations.

7 Conclusions

Using a machine learning based analysis, an integral flux sensitivity of 9.1 % in units of the Crab Nebula Flux for a five sigma detection in 50 h of observation time has been achieved. The Crab Nebula was detected with a statistical significance of 57.7 sigma in 91.1 h of observation time and the unfolded spectral energy distrubution is in agreement with the other IACT Experiments.

References

1. H. Anderhub, et al., Journal of Instrumentation **8**(06) (2013). DOI 10.1088/1748-0221/8/06/P06008

2. F. Temme, et al., Galaxies **5**(1) (2017). DOI 10.3390/galaxies5010018

3. A. Biland, et al., Journal of Instrumentation **9**(10) (2014). DOI 10.1088/1748-0221/9/10/P10012

4. M.L. Ahnen, et al., Astroparticle Physics **82**, 56 (2016)

5. V.P. Fomin, et al., Astroparticle Physics **2**(2), 137 (1994)

6. D. Heck, et al., Corsika: A monte carlo code to simulate extensive air showers. Tech. Rep. FZKA 6019, Forschungszentrum Karlsruhe (1998)

7. T. Bretz, D. Dorner, in *Proceedings of the 31st ICRC* (2009)

8. C. Bockermann, et al., in *Proceedings of the European Conference on Machine Learning (ECML), Industrial Track* (Springer Berlin Heidelberg, 2015)

9. M. Nöthe, et al. FACT-Tools version v1.0.0. DOI 10.5281/zenodo.1212390. URL https://github.com/fact-project/fact-tools/releases/v1.0.0

10. S. Ritt, *DRS4 datasheet rev. 0.9.* URL https://www.psi.ch/drs/DocumentationEN/DRS4_rev09.pdf

11. A.M. Hillas, in *19th International Cosmic Ray Conference*, vol. 3 (1985), vol. 3

12. K.A. Brügge, J. Buß, M. Nöthe. aict-tools version v0.12.0. URL https://github.com/fact-project/aict-tools

13. F. Pedregosa, et al., Journal of Machine Learning Research **12**, 2825 (2011)

14. R. Lessard, J. Buckley, V. Connaughton, S. Le Bohec, Astroparticle Physics **15**(1), 1 (2001)

15. T.P. Li, Y.Q. Ma, The Astrophysical Journal **272**, 317 (1983)

16. M. Börner, M. Nöthe, J. Bieker. funfolding version v0.2.0. URL https://github.com/tudo-astroparticlephysics/funfolding

17. M. Börner, Bestimmung des Energiespektrums von atmosphärischen Myonneutrinos mit 3 Jahren Daten des IceCube-Detektors. Ph.D. thesis, TU Dortmund (2018)

18. V. Blobel, arXiv preprint hep-ex/0208022 (2002)

19. M. Nöthe. fact_funfolding version v0.1.5. URL https://github.com/fact-project/fact_funfolding

20. D. Foreman-Mackey, D.W. Hogg, D. Lang, J. Goodman, PASP **125**, 306 (2013). DOI 10.1086/670067

21. D. Foreman-Mackey, D.W. Hogg, D. Lang, J. Goodman. emcee version v3.0rc1. DOI 10.5281/zenodo.1297477. URL https://github.com/dfm/emcee

22. J. Aleksić, et al., Journal of High Energy Astrophysics **5**, 30 (2015)

23. F. Aharonian, et al., The Astrophysical Journal **614**(2), 897 (2004)